Efficient production and transport of OH radicals in spatial afterglow of atmospheric-pressure DC glow discharge using intersecting helium flows

Naoki Shirai, Hiroki Owada and Koichi Sasaki

Division of Applied Quantum Science and Engineering, Hokkaido University, Japan

E-mail: nshirai@qe.eng.hokudai.ac.jp

September 2021

Abstract. An efficient method for generating OH radicals in the spatial afterglow of atmospheric-pressure plasma was investigated. The method employed a DC glow discharge along intersecting two helium flows in air. Tiny helium flows were ejected from two metal nozzles with inner diameters of 0.5 mm, and they intersected at a distance of 3-5 mm from the nozzles. A stable glow discharge was formed along the intersecting helium flows by applying a DC high voltage between the two nozzles. It was shown by laser-induced fluorescence spectroscopy that an origin of OH radicals was water vapor admixed into the intersection point of the two helium flows from ambient air. OH radicals were transported from the intersection toward the spatial afterglow along the coalesced helium flow. This is a distinctive feature of the present plasma source, by which we can obtain the stream of OH radicals in the outside of the active plasma zone even though we employ the DC discharge. In addition, we observed the production of OH radicals in the spatial afterglow. We presume that the production process of OH radicals in the spatial afterglow is dissociative electron attachment to H_2O_2.

1. Introduction

Atmospheric-pressure plasmas have been used for many applications [1–6]. Jet-type plasmas produced in air are especially useful in many applications since they can irradiate plasmas and/or the stream of radicals onto the surfaces of various materials including liquids and biological tissues [7–9]. In the last two decades, technologies for generating atmospheric-pressure plasma jets have achieved the remarkable progress.

Many plasma jet sources developed to date employ dielectric barrier discharges (DBDs) which are driven by AC and RF voltages [10–13]. The geometry of DBD which is developed by Teschke and coworkers is well-suited to plasma jets in air because of the easy transport of plasma and/or radicals to the outside of the discharge zone [14]. There are also reports which combine DBD plasma jets with multiple gas flows to generate plasmas for large-area processing [15–19]. However, the DBD-type plasma sources have limitations in the power deposition. DBD-type atmospheric-pressure plasma jets using

helium flows have electron temperatures less than 1 eV and electron densities on the order of 10^{11} cm^{-3} [20, 21]. The low electron density is caused by the limited power deposition, which may result in low densities of reactive radicals. On the other hand, it is possible to generate DC glow discharges at the atmospheric pressure by using ballast resistors [22–24]. The power deposition in the DC glow discharge is more efficient than that in DBD. An atmospheric-pressure DC glow discharge along the helium flow has an electron temperature of 2-3 eV and an electron density on the order of 10^{13}-10^{14} cm^{-3} [25–28]. It is also possible to generate a DC glow discharge between a metal electrode and the surface of liquid, which provides us a platform for investigating the plasma-liquid interaction [29, 30].

In the conventional geometry of the DC glow discharge in air, the high voltage for generating the discharge is applied between two electrodes, and the gas flow is usually parallel to the electric field. In this case, it is difficult to transport plasma and/or radicals to the outside of the discharge zone. In previous works, we proposed another geometry of DC glow discharge which utilized intersecting two helium flows [31,32]. The route of the discharge was not parallel to the electric field and we observed a kinked discharge along the intersecting two helium flows. The downward helium flow from the intersection point is realized in this geometry, and we can expect the transport of radicals from the discharge zone along the downward helium flow. In other words, we can realize a jet-type plasma source using this geometry even if we employ the DC glow discharge. An advantage of the DC discharge is the higher power deposition and the higher radical density than DBD plasma jets. In fact, Oh and coworkers observed high concentrations of various chemicals including H_2O_2 in the water irradiated with the downward flow from the intersection of the two helium flows [33], suggesting the efficient transport of radicals toward the water surface.

In this study, we measured the distribution of OH radical density in the DC-driven atmospheric-pressure glow discharge with intersecting helium flows by laser-induced fluorescence (LIF) spectroscopy. To obtain the accurate spatial distribution of the OH radical density, we also measured the spatial distributions of the rotational temperature of OH($X^2\Pi$) and the quenching frequency of laser-excited OH($A^2\Sigma^+$). The spatial distributions of the OH radical densities were examined at various discharge currents and gas flow rates. On the basis of the experimental results, we investigated the production and transport processes of OH radicals.

2. Experimental procedures

2.1. Plasma source

The plasma source used in this work was identical to that in our previous works [31,32]. All the experiments were carried out in the laboratory atmosphere. The temperature in the laboratory at the time of the experiment was 23 °C and the humidity was 45%.

Figure 1 shows a photograph of the atmospheric-pressure DC glow discharge with

intersecting two helium flows. The flows of helium were provided from two nozzle electrodes with inner and outer diameters of 0.5 and 0.8 mm, respectively. The distance between the tips of the two nozzle electrodes were 2-3.5 mm, and the two helium flows intersected at a distance of 3-5 mm from the nozzles at an angle of 45°. The gas flow rates were 400-800 sccm. A DC power supply was connected between the two electrodes via a limiting resistor of 500 kΩ. When a DC high voltage was applied, a glow discharge was generated along the intersecting helium flows, as shown in Fig. 1. The positive column, the Faraday dark space, and the negative glow, which were the features of DC-driven glow discharges, were observed by naked eyes. The range of the discharge current was 6-15 mA in this experiment.

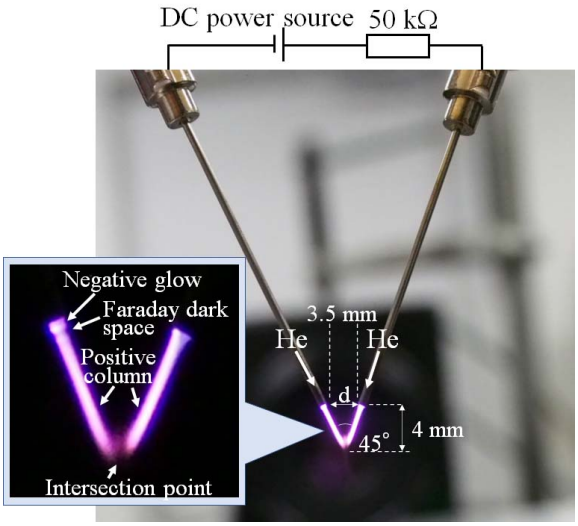

Figure 1. Photograph of atmospheric-pressure DC glow discharge using intersecting two helium flows. Two metal nozzles for the helium flows were connected to a DC power supply via a current-limiting resistor.

2.2. Laser-induced fluorescence

We used LIF imaging spectroscopy for measuring the spatial distribution of the OH radical density. The measurement method was similar to that in our previous works except the laser wavelength for exciting OH radicals [34, 35]. The light source for the LIF measurement was a pulsed tunable dye laser. The wavelength of the dye laser was tuned around 261.50 nm, by which OH radicals at the ground state $[X^2\Pi(v''=0)]$ were excited to the $A^2\Sigma^+(v'=2)$ state. We employed the $v''=0 \rightarrow v'=2$ excitation scheme since it was easier to suppress the stray light in the LIF image than the $v''=0 \rightarrow v'=1$ excitation scheme. The energy of the laser pulse was approximately 5.5 mJ. The shape of the laser beam was arranged to be planar using a cylindrical lens to illuminate the discharge space uniformly. The thickness of the planar laser beam was 0.5 mm, while the width of the planar laser beam was slightly wider than 10 mm. The intensity of the planar laser beam was sufficient to realize the saturation of the excitation, which

was confirmed by measuring the LIF intensity as a function of the laser intensity. The planar laser beam was injected from two directions, as shown in Fig. 2. In the optical arrangement shown in Fig. 2(a), the laser beam passed through the two plasma columns and the intersection of the two helium flows. On the other hand, the planar laser beam passed through the midway between the plasma columns in the arrangement shown in Fig. 2(b), and in this case OH radicals at the intersection of the two helium flows and in the spatial afterglow were detected.

The laser-induced fluorescence yielded by the spontaneous transitions from $A^2\Sigma^+(v' = 2)$ to $X^2\Pi(v'' = 2)$, from $A^2\Sigma^+(v' = 1)$ to $X^2\Pi(v'' = 1)$, and from $A^2\Sigma^+(v' = 0)$ to $X^2\Pi(v'' = 0)$ were captured using a charge coupled device camera with an image intensifier (ICCD camera). The transitions from $A^2\Sigma^+(v' = 2)$ to $A^2\Sigma^+(v' = 1)$ and $A^2\Sigma^+(v' = 0)$ were caused by vibrational energy transfer in the atmospheric pressure [13, 36]. An interference filter, which had the transmission at 310 ± 10 nm, was placed in front of the ICCD camera to discriminate LIF from the stray laser light and the self-emission of the plasma. We adjusted the gate width of the ICCD camera at $\Delta t = 120$ ns. The LIF images were accumulated for 200 laser shots on the ICCD camera to compensate the poor shot-to-shot reproducibility.

As has been reported in our previous work [34], the LIF image does not represent the spatial distribution of the OH density in atmospheric-pressure plasmas, since it is affected by the spatial distributions of the collisional quenching frequency of laser-excited $\mathrm{OH}(A^2\Sigma^+)$ and the rotational temperature of $\mathrm{OH}(X^2\Pi)$. We assume that the temporal variation of the LIF intensity, which is obtained by the excitation from a rotational state with a rotational quantum number J'', has the following waveform after the extinction of the laser pulse,

$$I_{J''}(t) = I^0_{J''} \exp\left(-\frac{t}{\tau}\right), \tag{1}$$

where $I^0_{J''} = I_{J''}(t = 0)$ means the initial value. The decay time constant τ is determined by the transition probability A and the collisional quenching frequency ν_q such that $1/\tau = A + \nu_\mathrm{q}$. The signal recorded at a pixel of the ICCD camera is given by the following equation,

$$S_{J''}(t) = \int_t^{t+\Delta t} I_{J''}(t')\mathrm{d}t' = \frac{I^0_{J''}}{A+\nu_\mathrm{q}}\Big[1-\exp(-(A+\nu_\mathrm{q})\Delta t)\Big]\exp\left(-(A+\nu_\mathrm{q})t\right). \tag{2}$$

Since the population density of the initial energy state, which is a rotational state of $\mathrm{OH}(X^2\Pi(v'' = 0))$ with a rotational quantum number J'', is proportional to $I^0_{J''}/A$, the relative density of the rotational state is obtained by

$$n_\mathrm{OH}(J'') \propto (1 + \frac{\nu_\mathrm{q}}{A})S_{J''}(t = 0). \tag{3}$$

The transition probabilities are given in literature to be 1.5×10^6, 8.6×10^5, and 4.5×10^5 s^{-1} for the $(v', v'') = (0, 0)$, $(1, 1)$, and $(2, 2)$ transitions, respectively [37].

Although the rate coefficients for collisional quenching by various molecules have been reported in [36, 38–40], we have to evaluate ν_q experimentally, since it is difficult to

know the spatial distribution of the composition of molecular species in the observation region. We evaluated $\nu_{\rm q}$ by measuring $S_{J''}(t)$ as a function of the delay time t after the extinction of the laser pulse. On the other hand, we measured $S_{J''}$ at the Q branch excitations from $J'' = 2$, 7 and 9 [41]. The spatial distribution of the rotational temperature $T_{\rm r}$ was evaluated from the relationship between $S^0_{J''}/(2J''+1)$ and $B_0 hcJ''(J''+1)$ (the Boltzmann plot) at each pixel of the ICCD camera, where h and c are the Plank constant and the speed of light, respectively, and B_0 is the rotational constant of OH($X^2\Pi$). By using $T_{\rm r}$, we estimated the total OH density from the relationship between the population density of a rotational state and the total OH density at the $X^2\Pi(v''=0)$ state [34].

2.3. Schlieren photography

The helium flows were visualized by schlieren photography, as shown in Fig 3. We used the schlieren system manufactured by Edmund Optics, which consisted of a lamp (the light source), two concave mirrors with focal lengths of 152 mm, a knife-edge, and a digital camera. The light from the lamp was collimated using a concave mirror, and the collimated light passed through the plasma. The light passed through the plasma was focused again using another concave mirror, but the focusing was not perfect since the wavefront of the light was distorted by the non-uniform refractive index around the plasma. Hence, by masking the light with the shifted focus using the knife-edge, we observed the unevenness of the refractive index as the gradation image of the light intensity on the digital camera. The photograph thus obtained represented the image of the flow around the plasma. We placed the plasma columns in the two ways as illustrated in Fig 3, by which we observed the front and side views of the flow.

2.4. Detection of electrical current in spatial afterglow

It was necessary to examine the existence of electrical charges in the spatial afterglow to discuss the kinetics of OH radicals. To measure the electrical current passing through the spatial afterglow, we placed a planar electrode at various distances from the intersection of the two helium flows, as shown in Fig. 4. The planar electrode was connected to the electrical ground via a resistor, and the current was obtained by measuring the voltage drop at the resistor. We employed 150 kΩ for the resistor.

3. Results

3.1. Images of self-emission and laser-induced fluorescence

The image of the self-emission of the plasma was captured using the ICCD camera via the interference filter, as shown in Fig. 5(a). The optical arrangement shown in Fig. 2(a) was used for taking this image. The voltage between the two electrodes, the discharge current, the flow rate of helium, and the distance between the two electrodes were 0.8

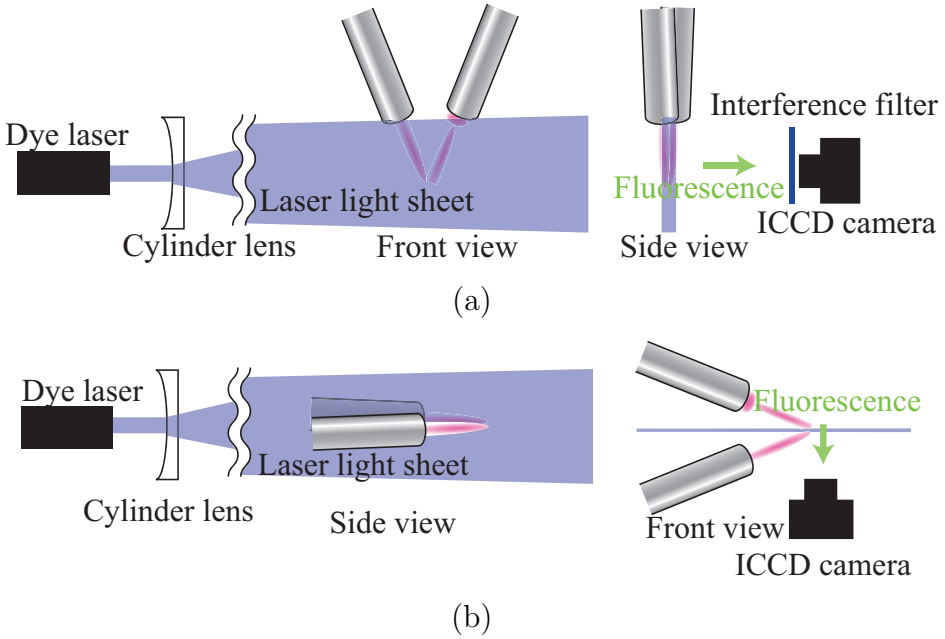

Figure 2. Optical arrangements for LIF imaging spectroscopy. The tunable dye laser beam passed through the two plasma columns in the optical arrangement shown in (a), whereas the laser beam passed through the midway between the two plasma columns in (b).

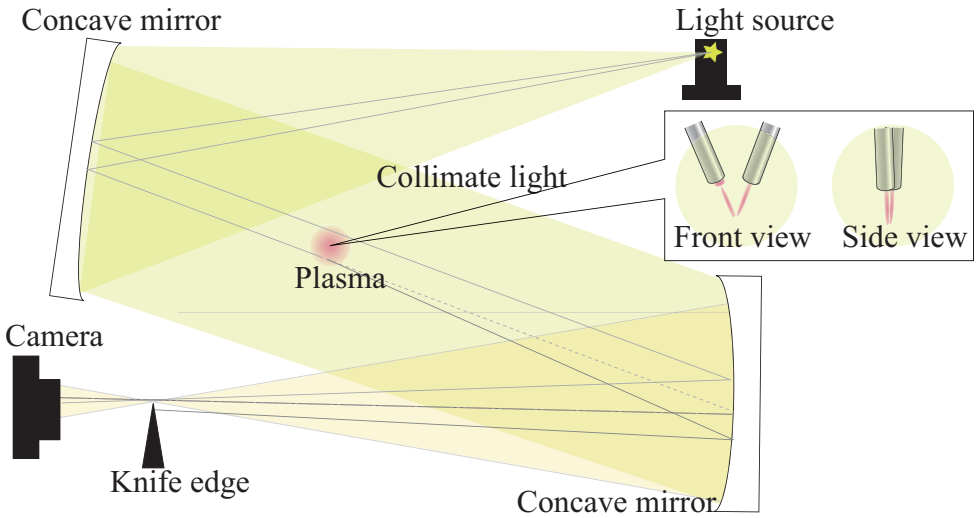

Figure 3. Optical arrangement for schlieren photography. The plasma was placed in the pass way of the collimated light in two ways illustrated in the figure.

kV, 6 mA, 800 sccm, and 3.5 mm, respectively. As shown in the figure, the optical emission was observed along the intersecting helium flows, and we observed no optical emission from the spatial afterglow region below the intersection point. Figure 5(b) shows the LIF image observed at the same discharge conditions as those in Fig. 5(a). This image was obtained when we opened the gate of the ICCD camera just before the injection of the dye laser pulse. The origin of the delay time t is defined by this timing

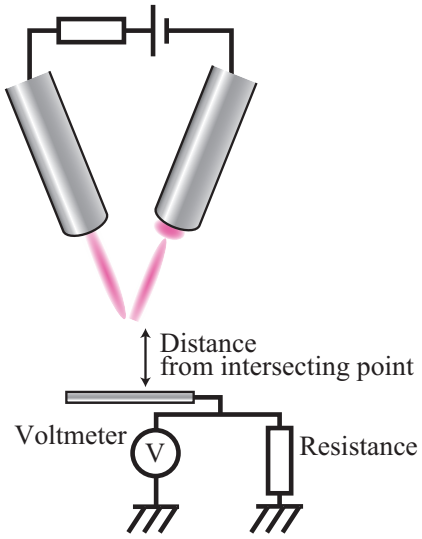

Figure 4. Method for measuring electrical current in spatial afterglow.

in this paper. We observed the clear LIF image below the intersection of the two helium flows, as shown in Figure 5(b), indicating the existence of OH radicals in the spatial afterglow.

3.2. Evaluations of collisional quenching frequency and rotational temperature

We took the LIF images at various delay times, and we plotted the temporal variation of the LIF intensity [$S_{J''}(t)$ in Eq. (2)] at each pixel of the ICCD camera. Figure 6 shows representative temporal variations which were observed at the three positions indicated in the LIF image (at the intersection of the two helium flows, at a point in the discharge column, and at a point in the spatial afterglow). Exponential decays in the LIF intensities were observed, as shown in Fig. 6, and the values of $A + \nu_q$ were evaluated from the time constants of the exponential decreases. We evaluated the decay time constant at each pixel of the ICCD camera, and obtained the two-dimensional map of the decay frequency of laser-excited OH($A^2\Sigma^+$). Figure 7 shows the Boltzmann plots observed at the intersection of the two helium flows and a point in the discharge column. The slopes of the Boltzmann plots represent the rotational temperatures T_r, as indicated in Fig. 7. The error in the evaluation of the rotational temperature was estimated to be approximately $\pm 10\%$ on the basis of the ambiguity in the Boltzmann fitting. The similar Boltzmann fitting was repeated at each pixel of the ICCD camera, and we obtained the two-dimensional map of the rotational temperature.

3.3. Distributions of rotational temperature, collisional quenching frequency, and OH radical density

Figures 8(a), 8(b), and 8(c) show the two-dimensional distributions of the rotational temperature of OH($X^2\Pi(v'' = 0)$), the collisional quenching frequency of OH($A^2\Sigma^+$),

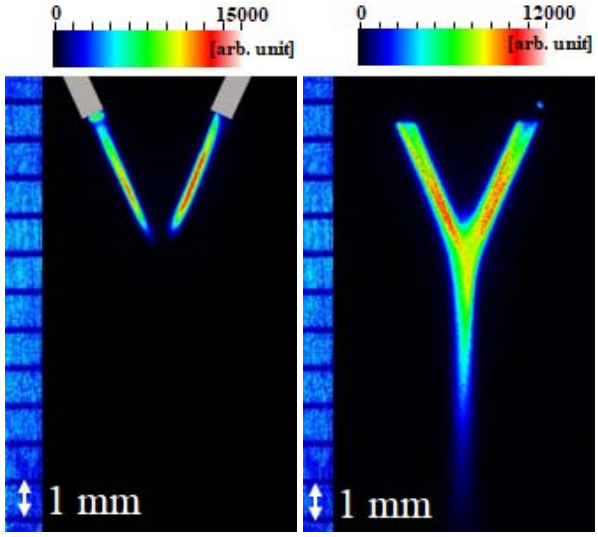

Figure 5. Typical images of (a) optical emission of plasma and (b) LIF intensity.

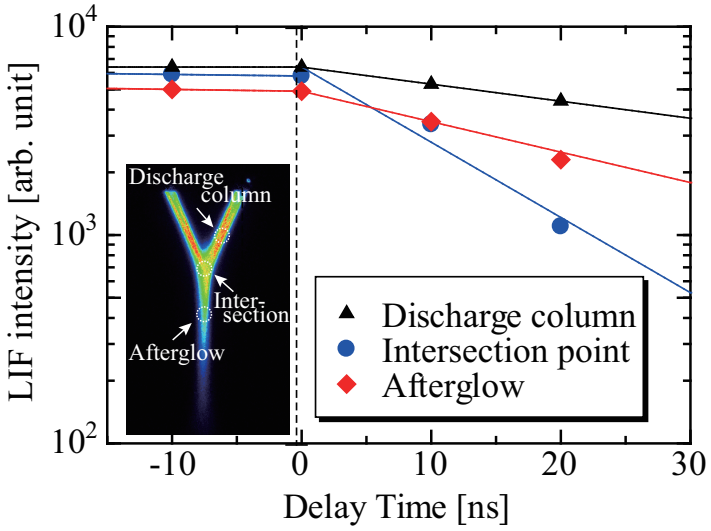

Figure 6. Temporal variations of the LIF intensity at three positions illustrated in the LIF image.

and the OH density, respectively. The discharge conditions were the same as those in Fig. 5. As shown in Fig. 8(a), the rotational temperature was 400 K in the cores of the helium flows, and it was approximately 500 K in the surrounding part of the helium flows and the spatial afterglow. On the other hand, we observed the significant spatial distribution of the collisional quenching frequency, as shown in Fig. 8(b). The collisional quenching frequency was low in the plasma columns or the cores of the helium flows, whereas a high frequency of collisional quenching was observed in the spatial afterglow. The spatial distribution of the OH density was reconstructed as shown in Fig. 8(c) by taking into consideration the spatial distributions of the rotational temperature (Fig. 8(a)) and the collisional quenching frequency(Fig. 8(b)). Note that the spatial

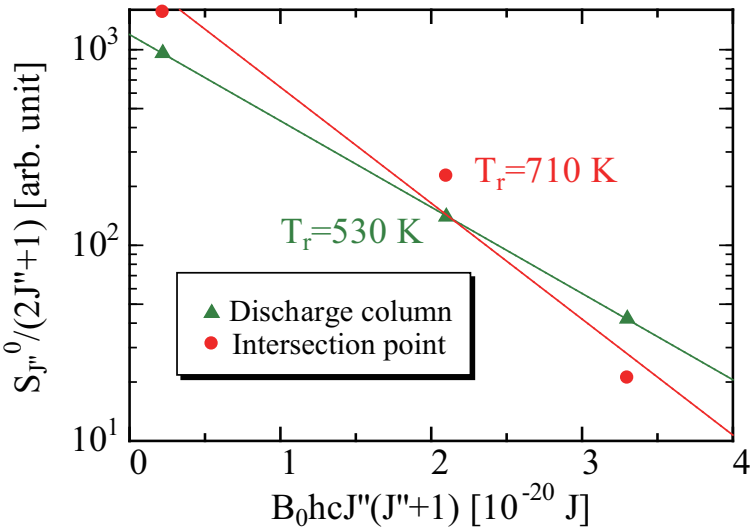

Figure 7. Boltzmann plots obtained at the intersection of the two helium flows and at a point in the discharge column.

distribution of the OH density is remarkably different from the LIF image shown in Fig. 5(b). The LIF intensity in the plasma columns was strong, but the OH density in the plasma columns, especially in the cores of the helium flows, was extremely low. The peak of the OH density was located at the intersection of the two helium flows. The LIF intensity in the spatial afterglow at a distance of 7 mm from the intersection point was negligible, but we observed the considerable OH density at the same position.

Figures 9(a)-9(d) show the distributions of the optical emission intensity, the rotational temperature, the collisional quenching frequency, and the OH density, when the flow rate of helium was 400 sccm. The other discharge conditions were the same as those in Figs. 5 and 8. By comparing Fig. 8 with Fig. 9, we understood that the smaller helium flow rate changed the discharge as follows. 1) The lengths of the plasma columns with optical emission became shorter, 2) the rotational temperature at the intersection of the two helium flows became higher, 3) the collisional quenching frequency at the intersection point and the spatial afterglow became higher, and 4) the OH density at the intersection point became higher. In addition, the spatial decay of the OH density in the spatial afterglow was more significant, and the diameter of the region with OH radicals in the spatial afterglow was wider at the flow rate of 400 sccm.

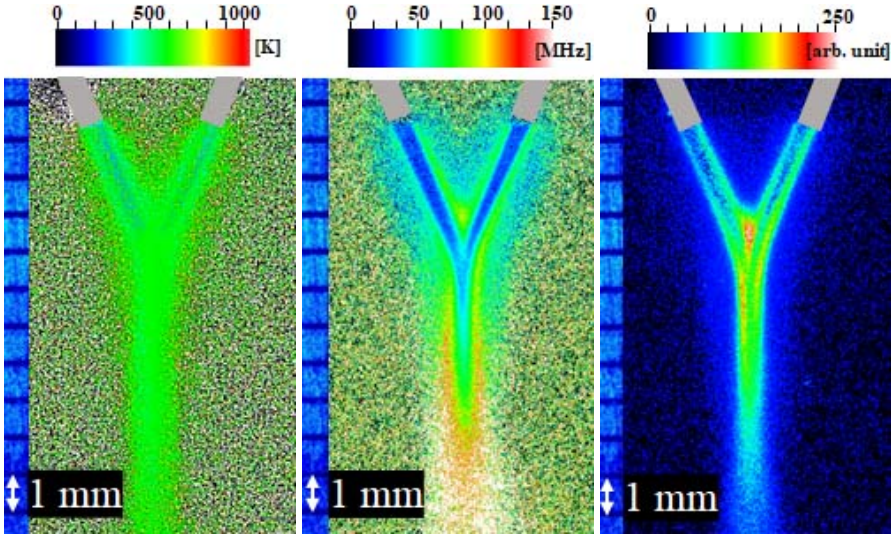

(a) (b) (c)

Figure 8. Two dimensional maps of (a) rotational temperature of OH($X^2\Pi(v'' = 0)$), (b) destruction frequency of laser-excited OH($A^2\Sigma^+$), and (c) OH radical density. The discharge conditions were the same as those in Fig. 5.

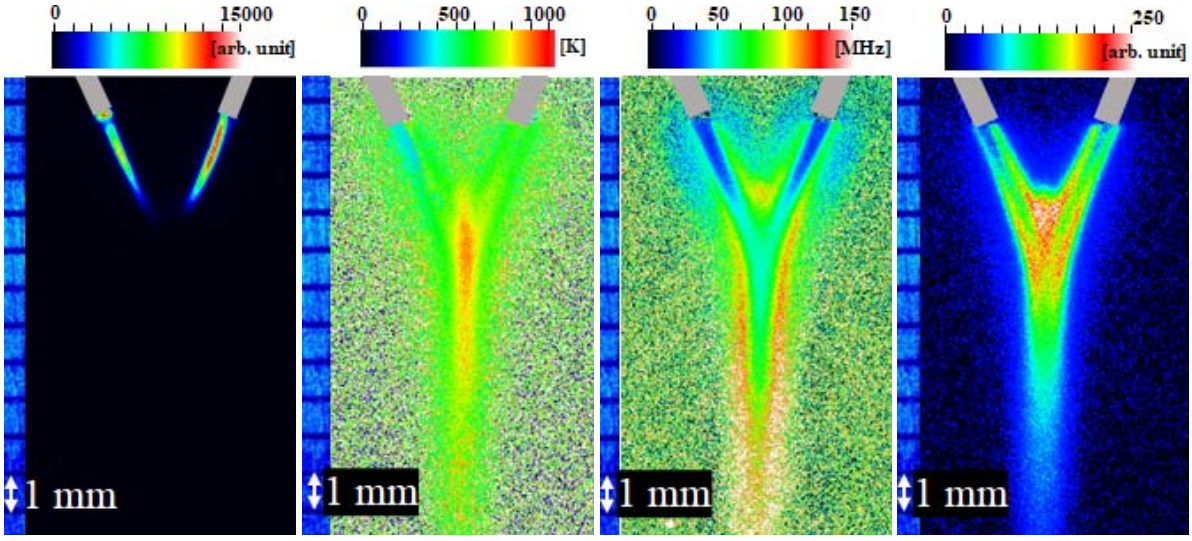

(a) (b) (c) (d)

Figure 9. Two dimensional maps of (a) optical emission intensity, (b) rotational temperature of OH($X^2\Pi(v'' = 0)$), (c) destruction frequency of laser-excited OH($A^2\Sigma^+$), and (d) OH radical density, when the flow rate of helium was changed to 400 sccm. The other discharge conditions were the same as those in Fig. 8.

Figure 10 shows the distributions of the OH radical density at three discharge currents. The OH density in the discharge columns was roughly independent of the discharge current or the discharge power, whereas we observed the increase in the OH density with the discharge current at the intersection of the two helium flows. The OH density in the spatial afterglow also increased slightly with the discharge current. In addition, the radial distribution of the OH density in the spatial afterglow was fattened by the increase in the discharge current.

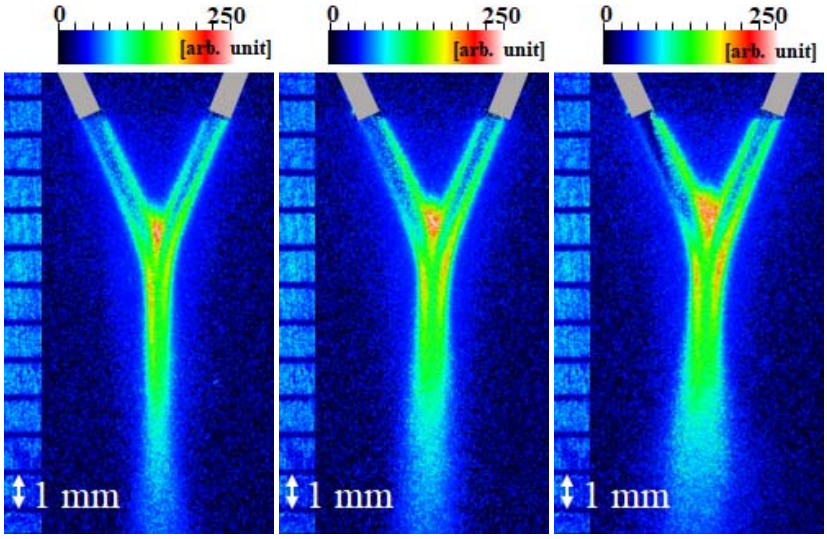

Figure 10. Two-dimensional distributions of OH radical density at discharge currents of (a) 6, (b) 9, and (c) 12 mA. Flow rate of helium was 800 sccm.

Figure 11 shows the distributions of the OH density when they were observed using the optical arrangement shown in Fig. 2(b). The helium flow rates were 800 and 400 sccm in Figs. 11(a) and 11(b), respectively, and the other discharge conditions were the same as those in Figs. 8 and 9. It is seen from this figure that OH radicals spread over a wider region in the direction perpendicular to the images shown in Figs. 8 and 9. A remarkable distribution was observed at a flow rate of 800 sccm (Fig. 11(a)), where we observed the second peak of the OH density at a distance of 3 mm from the intersection of the two helium flows.

3.4. Schlieren images

Figures 12(a) and 12(b) show the front and side views of the schlieren photographs, respectively. The helium flow rate was 800 sccm and the discharge current was 12 mA. The images of the helium flows represented by the schlieren photographs were similar to the distributions of the OH radical density shown in Figs. 8, 9, and 11. However, it is known by taking a closer look at Fig. 12 that the region with flows around the plasma columns and the intersection of the two helium flows was broader than the distribution of the OH density, indicating that the flows were induced in ambient air by the discharge.

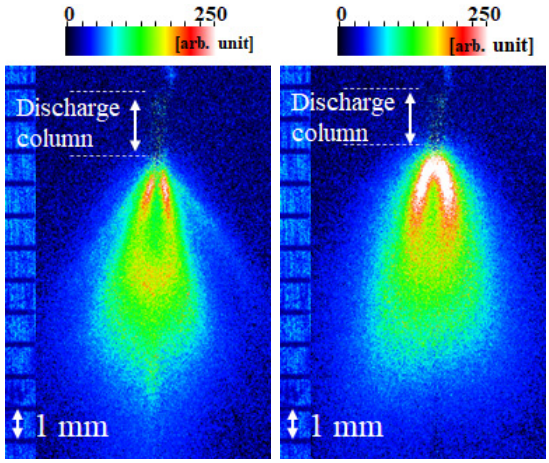

Figure 11. Distribution of OH radical density observed using optical arrangement shown in Fig. 2(b). Flow rates of helium were (a) 800 and (b) 400 sccm.

In addition, the length of the downward helium flow below the intersection point was longer than the distribution of the OH density. It is seen from the schlieren photographs that the flow induced around the plasma was turbulent.

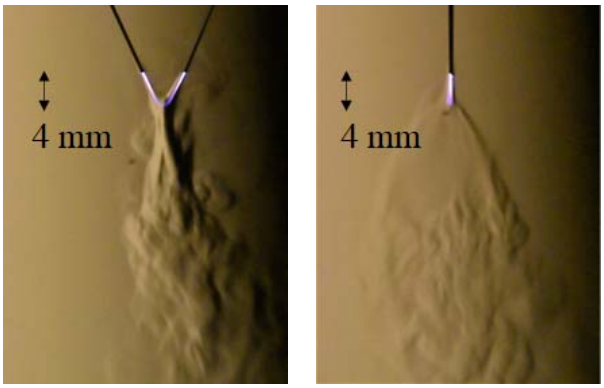

Figure 12. Schlieren photographs showing the images of gas flow. Flow rate of helium was 800 sccm. (a) and (b) were observed by placing the two plasma columns in the perpendicular and parallel directions to the collimated light, as shown in Fig. 3.

3.5. Current in spatial afterglow

Figure 13 shows the result of the electrical current measurement in the spatial afterglow. The flow rate of helium was 800 sccm, the discharge current was 6 mA, and the voltage between the two electrodes was 830 V. The current at a distance of 1.5 mm from the intersection point was approximately 7.2 μA, which was 10^{-3} times smaller than the current passing through the discharge columns.

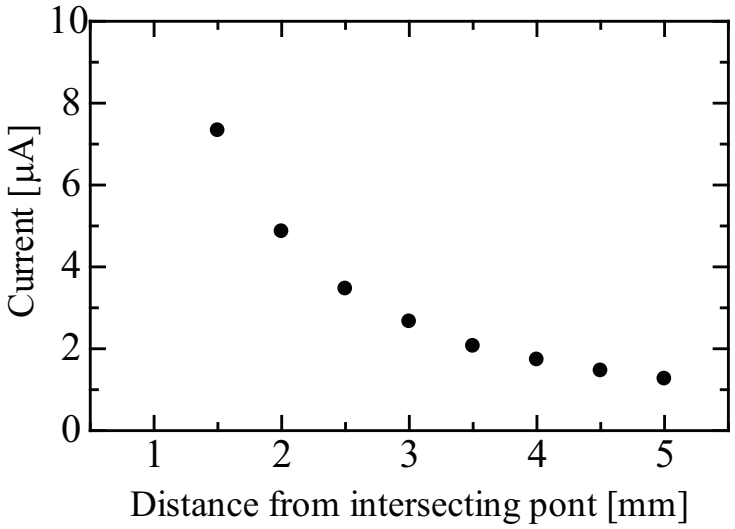

Figure 13. Electrical current detected in spatial afterglow as a function of the distance from the intersection of the two helium flows.

4. Discussion

4.1. Destruction processes of laser-excited OH($A^2\Sigma^+$)

The decay time constant of the LIF intensity, which is proportional to the density of laser-excited OH($A^2\Sigma^+$), is much shorter than the reciprocal of the transition probability, as shown in Fig. 6, indicating that the loss process of OH($A^2\Sigma^+$) is dominated by collisional quenching. According to the paper published by Martini and coworkers [36], the rate coefficients for collisional quenching of OH($A^2\Sigma^+, v' = 1$) by N_2, O_2, and H_2O are 2.7×10^{-10}, 2.4×10^{-10}, and 6.1×10^{-10} cm^3/s, respectively. The rate coefficient for quenching by collision with helium is negligible in comparison with those by N_2, O_2, and H_2O. On the other hand, the rate coefficients for the vibrational energy transfer from OH($A^2\Sigma^+, v' = 1$) to OH($A^2\Sigma^+, v' = 0$) by collision with N_2 and O_2 are 2.1×10^{-10} and 2.3×10^{-11} cm^3/s, respectively. Although the rate coefficients for OH($A^2\Sigma^+, v' = 2$) are not available to date, it may be reasonable to assume similar rate coefficients for OH($A^2\Sigma^+, v' = 1$) and OH($A^2\Sigma^+, v' = 2$). Under this assumption, it is expected that laser-excited OH($A^2\Sigma^+, v' = 2$) is quenched quickly if molecular species in air are admixed into the helium flow, and in addition, a part of OH($A^2\Sigma^+, v' = 2$) is transferred to OH($A^2\Sigma^+, v' = 0$) and OH($A^2\Sigma^+, v' = 1$). The production of OH($A^2\Sigma^+, v' = 1$) is temporal, and it is finally transferred to OH($A^2\Sigma^+, v' = 0$). The rate coefficients for collisional quenching of OH($A^2\Sigma^+, v' = 0$) are smaller than those of OH($A^2\Sigma^+, v' = 1$), and they are 3.8×10^{-11}, 1.4×10^{-10}, and 6.6×10^{-10} cm^3/s for N_2, O_2, and H_2O, respectively. Therefore, OH($A^2\Sigma^+, v' = 0$) produced by the vibrational energy transfer has a longer lifetime, and the quenching frequencies we observed in this experiment with a gate width of $\Delta t = 120$ ns (Figs. 8(b) and 9(c)) mainly represent the lifetime of OH($A^2\Sigma^+, v' = 0$). According to the rate coefficients for collisional

quenching of OH($A^2\Sigma^+, v' = 0$), the quenching frequency of 10^8 s^{-1} corresponds to the partial pressure of 10 kPa for the air components admixed into the helium flows, if we ignore the contribution of H_2O to the collisional quenching process.

4.2. Mixing of air into helium flows and production process of OH in discharge columns

Because of the dominant collisional quenching by N_2, O_2, and H_2O, the spatial distributions of the collisional quenching frequency shown in Figs. 8(b) and 9(c) represent the density distributions of air components admixed into the helium flows. It is understood from Fig. 8(b) that the regions of the two discharge columns are occupied by the helium flows. The admixture of ambient air into the helium flow is greater at the intersection of the two helium flows, and the high densities of the air components are observed in the downstream of the spatial afterglow. The schlieren image shown in Fig. 12 clearly shows the turbulent flow in ambient air around the plasma columns, which may enhance the admixture of air into the intersection point.

The distributions of the OH density in the discharge columns and the intersection of the two helium flows are understood by the admixture of ambient air. The rate coefficient for electron impact dissociation of H_2O ($H_2O + e \rightarrow OH + H + e$) is affected by the electron temperature significantly, and the electron temperature is high in the discharge columns with optical emissions. However, the production rate of OH is low in the discharge columns because of the negligible H_2O density or the occupation by helium. Although the optical emission image shown in Fig. 5(a) suggests that the electron temperature at the intersection point is lower than that in the discharge columns, the intersection point works as the main production area of OH via electron impact dissociation of H_2O because of the greater admixture of ambient air. The importance of the admixture of ambient air is understood by the comparison between Figs. 8 and 9. As shown in Fig. 9(c), the decrease in the helium flow rate induces the more significant admixture of the air components at around the intersection point, resulting in the higher OH density. In addition, the experimental result shown in Fig. 10 is understood to be due to the increase in the electron density with the discharge current. Accordingly, the distribution of the OH density and its dependences on the helium flow rate and the discharge current is consistent with the dominant production of OH by electron impact dissociation of H_2O.

4.3. Transport of OH radicals to spatial afterglow

The experimental results clearly indicate the existence of OH radicals in the spatial afterglow. This is a distinctive feature of the plasma source used in this experiment in comparison with other plasma jet sources, where the areas with OH radicals are roughly the same as the jet regions with optical emissions [10–12]. By comparing the schlieren photographs shown in Fig. 12 with the distributions of the OH densities shown in Figs. 8(c) and 11, it is understood that OH radicals in the spatial afterglow are transported from the intersection point along the coalesced helium flow. The shape

of the discharge columns or the route of the electrical current is determined by the combined effect of the spatial distributions of the helium density and the electrical potential, but the shape of the gas flow is not affected by the electrical potential. The intersecting helium flows are effective to induce the downward transport of OH radicals. Since the flow speed of helium is estimated to be 20 m/s, the transport length of 6 mm corresponds to the lifetime of 0.3 ms for OH radicals. The dominant loss process of OH is considered to be three-body association $OH + OH + M \rightarrow H_2O_2 + M$. Since the rate coefficient for this reaction is 1.7×10^{-11} cm^3/s at the atmospheric pressure [42], the lifetime of 0.3 ms suggests the OH density of 2×10^{14} cm^{-3}.

4.4. Production process of OH in the spatial afterglow

Although the experimental results show the importance of the transport of OH radicals into the spatial afterglow, the spatial distribution of the OH density is not determined only by the transport, and we should consider another process to explain the OH radical density in the spatial afterglow. An evidence is the spatial distribution shown in Fig. 11(a), where the OH density has the second peak at a distance of 3 mm from the intersection of the two helium flows. This distribution reveals the production of OH radicals in the spatial afterglow area.

The experimental result shown in Fig. 13 suggests a plasma flow in the spatial afterglow. A possible mechanism is the viscous transport with the coalesced helium flow. Therefore, there is a possibility that electrons are available in the spatial afterglow.

As shown in the photograph of the discharge, the optical emission intensity was negligible in the spatial afterglow, indicating that the electronic excitation by the impact of energetic electrons was not available. Therefore, it is reasonable to suppose that the production of OH radicals by electron impact dissociation of H_2O does not work in the spatial afterglow. In addition, since dissociative electron attachment to H_2O ($H_2O + e \rightarrow OH + H^-$) needs electrons with energies higher than 5.5 eV [43], the production of OH from H_2O by electron impact cannot be expected in the spatial afterglow.

A possible production process of OH in the spatial afterglow is Penning dissociation by the collision between H_2O and He^M (metastable state of helium) [44, 45]. However, considering the rate coefficient on the order of 10^{-10} cm^3/s for the collisional quenching by molecular nitrogen [46], the lifetime of He^M in the spatial afterglow is estimated to be shorter than 100 ns. This is because the partial pressure of the air components admixed into the helium flow is close to 10 kPa according to the collisional quenching frequency of $OH(A^2\Sigma^+, v' = 0)$ shown in Figs. 8(b) and 9(c). Therefore, it is considered that the transport of He^M into the spatial afterglow and the production of OH by Penning dissociation of H_2O are negligible.

In this paper, we propose dissociative electron attachment to H_2O_2 ($H_2O_2 + e \rightarrow OH + OH^-$) as a production process of OH in the spatial afterglow. According to Nandi and coworkers, dissociative electron attachment to H_2O_2 has a huge cross section on the

order of 10^{-17} cm^2 [47]. In addition, the cross section of dissociative electron attachment to H_2O_2 has the maximum at a low electron energy of 0.5 eV [47]. H_2O_2 is produced via $OH + OH + M \rightarrow H_2O_2 + M$. Therefore, dissociative electron attachment to H_2O_2 can work as a production process of OH in the spatial afterglow. In a previous work, we have suggested that the same reaction is active in an atmospheric-pressure glow discharge as a production process of OH^- [48].

4.5. Kinetics of gas temperature

Finally, we discuss the kinetics of gas temperature in the present plasma source. The rotational temperature of $OH(X^2\Pi(v'' = 0))$ can work as the representative of the gas temperature. Figure 8(a) shows a lower gas temperatures inside the cores of the helium flows. It is understood by comparing Figs. 8(a) and 8(b) that the distribution of the gas temperature is correlated with the air components admixed into the helium flows. The lower gas temperature in the helium flow is reasonable, since the energy transfer process from electrons to helium atoms is only elastic collision. In contrast, for molecular nitrogen and oxygen, the inelastic collision with electrons to produce vibrational excited states, followed by the vibrational-translational energy transfer can work as the additional gas heating process. This is a reason for the fact that the region with a larger amount of admixed air components has a higher gas temperature. This mechanism can explain the experimental result shown in Fig. 9(b), which indicates the increase in the gas temperature with the decrease in the flow rate of helium. In addition, the slower flow speed or the longer gas residence time in the discharge zone may be another mechanism for the higher gas temperature at the lower flow rate.

5. Conclusions

In this study, we investigated the density of OH radicals in an atmospheric-pressure DC glow discharge with intersecting two helium flows. The OH radical density was low in the discharge columns since they were occupied by helium ejected from the nozzle electrodes. The production of OH radicals was obtained dominantly in the intersection of the two helium flows, and the production process was electron impact dissociation of H_2O. The admixture of H_2O into the intersection, which was enhanced by the plasma-induced turbulent flow, was an important factor to obtain the high OH radical density. OH radicals produced in the intersection of the two helium flows were transported to the spatial afterglow along the coalesced helium flow. This was a distinctive feature of the present plasma source, by which we obtained the stream of OH radicals in the outside of the active plasma zone even though we employed the DC discharge between the two electrodes. In addition, we observed the additional production of OH radicals in the spatial afterglow. We presume that the production process of OH radicals in the spatial afterglow is dissociative electron attachment to H_2O_2 which is produced by three-body association of OH radicals. The present method for producing the stream of

OH radicals using the DC discharge has potential applications in various technologies which need the irradiation of OH radicals to liquids and other materials.

Acknowledgment

This work was supported by JSPS KAKENHI Grant Numbers 20H00135.

References

[1] P. Bruggeman and C. Leys: J. Phys. D **42** (2009) 053001.
[2] P. Bruggeman et al., Plasma Sources Sci. Technol. **25** (2016) 053002.
[3] G. Fridman, G. Friedman, A. Gutsol, A. Shekhter, V. Vasilets and A. Fridman, Plasma Process. Polym. **5** (2008) 503.
[4] I. Adamovich et al., J. Phys. D **50** (2017) 323001.
[5] K. Takaki, N. Hayashi, D. Wang and T. Ohshima, J. Phys. D **52** (2019) 473001.
[6] M. Kong, G. Kroesen, G. Morfill, T. Nosenko, T. Shimizu, J. Dijk and J. Zimmermann, New J. Phys. **11** (2009) 115012.
[7] A. Schutze, J. Jeong, S. Babayan, J Park, G. Selwyn and R. Hicks, IEEE Ttans. Plasma Sci. **26** (1998) 1685.
[8] M. Laroussi and T. Akan, Plasma Process. Polym., **4** (2007) 777.
[9] S. Reuter, Th. Woedtke and K. Weltmann, J. Phys. D: Appl. Phys. **51** (2018) 233001.
[10] X Pei Y Lu, S Wu, Q Xiong and X Lu, Plasma Sources Sci. Technol. **22** (2013) 025023.
[11] X. Pei, S. Wu, Y. Xian, X. Lu and Y. Pan, IEEE Trans.Plasma Sci. **42** (2014) 1206.
[12] T. Verreycken, R. Mensink, R. Horst, N. Sadeghi and P. Bruggeman, Plasma Sources Sci. Technol. **22** (2013) 055014.
[13] S. Yonemori, Y. Nakagawa, R. Ono and T. Oda, J. Phys. D: Appl. Phys. **45** (2012) 225202.
[14] M. Teschke, J. Kedzierski, E.G. Finantu-Dinu, D. Korzec, J. Engemann, IEEE Trans. Plasma Sci. **33** (2005) 310.
[15] M. Johnson, D. Boris, T. Petrova and S. Walton, Plasma Sources Sci. Technol. **29** (2020) 015006.
[16] M. Ghasemi, P. Olszewski, J.Bradley and J.Walsh, J. Phys. D **46** (2013) 052001.
[17] QY Nie, Z. Cao, C.Ren, D. Wang and M. Kong, New J. Phys. **11** (2009) 115015.
[18] C. Douat, M. Fleury, M. Laroussi and V. Puech, IEEE Trans. Plasma Sci. **39** (2011) 2298.
[19] C. Douat, G. Bauville, M. Fleury, M. Laroussi and V. Puech, Plasma Sources Sci. Technol. **21** (2012) 034010.
[20] Z. Chang, G. Zhang, X. Shao and Z. Zhang, Phys. Plasma **19** (2012) 073512.
[21] G. Sretenović, O. Guaitella, A. Sobota, I. Krstic, V. Kovacevic, B. Obradovic and M. Kuraica, J. Appl. Phys. **121** (2017) 123304.
[22] D. Staak, B. Farouk, A. Gutsol and A. Fridman Plasma Sources Sci. Technol. 14 (2005) 700.
[23] D. Staak, B. Farouk, A. Gutsol and A. Fridman Plasma Sources Sci. Tech. 15 (2006) 818.
[24] D. Staak, B. Farouk, A. Gutsol and A. Fridman, Plasma Sources Sci. Tech 17 (2008) 025013.
[25] K. Tomita, K. Urabe, N. Shirai, Y, Sato, S, Hassaballa, N. Bolouki, M. Yoneda, T. Shimizu and K. Uchino, Jpn. J. Appl. Phys. 55 (2016) 066101.
[26] K. Urabe, N. Shirai, K. Tomita, T. Akiyama and T. Murakami, Plasma Sources. Sci. Technol. 25 (2016) 045004.
[27] F. Tochikubo, N. Shirai and S. Uchida, Appl. Phys. Express 4 (2011) 056001.
[28] T. Farouk B. Farouk, D. Staack, A. Gutsol and A. Fridman, Plasma Sources Sci. Technol. 15 (2006) 676.
[29] N. Shirai, K. Ichinose, S. Uchida and F. Tochikubo: Plasma Sources Sci.Technol. **20** (2011) 034013.
[30] N. Shirai, S. Uchida, and F. Tochikubo: Plasma Sources Sci. Technol. **23** (2014) 054010.
[31] N. Shirai, S. Ibuka and S. Ishii, IEEE Trans. Plasma Sci. **36** (2008) 960.

[32] N. Shirai, H. Shito, S. Ibuka and S. Ishii, Appl. Phys. Express **2** (2009) 076001.
[33] J. OH, "International Study of Plasma Activated Water: Chemical Composition of RONS" 11th International Symposium on Advanced Plasma Science and its Applications for Nitrides and Nanomaterials / 12th International Conference on Plasma-Nano Technology and Science 2019
[34] H. Ishigame, S. Nishiyama and K. Sasaki, Jpn. J. Appl. Phys. **54** (2015) 01AF02.
[35] K. Sasaki, H. Ishigame and S. Nishiyama, Eur. Phys. J. Appl. Phys. **71** (2015) 20807
[36] L. Martini, N. Gatti, G. Dilecce, M. Scotoni and P. Tosi, J. Phys. D **50** (2017) 114003.
[37] J. Luque and D. Crosley, J. Chem. Phys. **109** (1998) 439.
[38] U. Rahmann, W. Kreutner and K. Kohse-Höinghaus, Appl. Phys. B **69** (1999) 61.
[39] L. Williams and D. Crosley, J. Chem. Phys. **104** (1996) 6507.
[40] M. Tamura, P. Berg, J. Harrington, J. Luque, J. Jeffries, G. Smith and D. Crosley, Combust. Flame **114** (1998) 502.
[41] K. Sasaki and S. Aoki Appl. Phys. Express **1** (2008) 086001.
[42] R. Atkinson, D. L. Baulch, R. A. Cox, R. F. Hampson, Jr., J. A. Kerrand and J. Troe, J. Phys. Chem. Ref. Data18(1989) 881.
[43] C. Melton and J. Chem. Phys. **57** (1972) 4218.
[44] D.Liu, P. Bruggeman, F. Iza, M. Rong and M. Kong, Plasma Sources Sci. Technol. **19** (2010) 025018
[45] C. Tschang, R. Bergert, S. Mitic and M. Thoma, J. Phys. D: Appl. Phys. **53** (2020) 215202
[46] W. Lindinger, A. L. Schmeltekopf and F. C. Fehsenfeld, J. Chem. Phys. **61** (1974) 2890.
[47] D. Nandi, E. Krishnakumar, A. Rosa, W. Schmidt and E. Illenberger, Chemical Physics Letters **373** (2003) 454.
[48] K. Sasaki, R. Hosoda and N. Shirai, Plasma Sources Sci. Technol. **29** (2020) 085012.